Materials Horizons

ROYAL SOCIETY OF CHEMISTRY

COMMUNICATION

View Article Online
View Journal



Cite this: DOI: 10.1039/d5mh01095k

Received 9th June 2025,
Accepted 31st July 2025

DOI: 10.1039/d5mh01095k

rsc.li/materials-horizons



# Ferroelectricity driven interlayer magnetic phase transitions in van der Waals homobilayers

Jiale Wang, Xinru Li,* Yibo Liu, Ying Dai,* Baibiao Huang and Yandong Ma*

**Exploring magnetoelectric coupling in bilayers represents a particularly intriguing topic in multiferroic physics, with current efforts predominantly focused on heterobilayer architectures. Herein, we present an unconventional approach to achieve electrically controlled interlayer magnetic phase switching in homobilayer systems. Our mechanism mediates reversible ferroelectrically driven transitions between antiferromagnetic (AFM) and ferromagnetic (FM) orders *via* polarization-dependent band engineering. The underlying mechanism stems from symmetry-broken interlayer charge transfer: antiparallel ferroelectric polarization enforces a parallel band configuration that stabilizes AFM interlayer coupling through local superexchange interactions, while parallel polarization creates type-III band alignment that satisfies the Stoner criterion and thus promotes FM interlayer ordering. Using first-principles, we demonstrate this paradigm in a $Tl_2NO_2$ homobilayer. Notably, the AFM phase hosts coexisting layer-polarized valley and spin Hall currents, whereas these novel features become mutually exclusive in the FM phase, enabling nonvolatile ferroelectric switching of both valley and spin degrees of freedom. This work establishes a fundamental design principle for creating electrically addressable two-dimensional multiferroics.**

### New concepts

We present a new strategy for achieving electrically controlled interlayer magnetic phase transitions in van der Waals homobilayers, unlocking a transformative pathway to nonvolatile multiferroicity. In contrast to conventional heterostructures, where interfacial asymmetry restricts transitions to ferromagnetic–ferrimagnetic (FM–FiM) states, our approach leverages ferroelectric polarization-mediated band engineering to enable fully reversible switching between antiferromagnetic (AFM) and FM orders. We reveal that the key innovation lies in symmetry-governed charge redistribution: antiparallel polarization induces momentum-matched band alignment, stabilizing AFM coupling *via* localized superexchange, while parallel polarization creates a type-III band offset, satisfying the Stoner criterion for delocalized FM ordering. First-principles calculations on $Tl_2NO_2$ reveal that the AFM phase hosts coexisting layer-polarized valley and spin Hall currents, whereas FM ordering suppresses these features, enabling all-electric control of topological quantum phenomena. This work establishes a paradigm for designing 2D multiferroics with electrically programmable spin and valley degrees of freedom.

## Introduction

Multiferroicity in coupled ferroelectric–(anti)ferromagnetic systems arises from symmetry-breaking quantum fluctuations that entangle electric polarization and magnetization *via* magnetoelectric coupling.[1,2] This emergent phenomenon holds transformative potential for next-generation electronics[3–5] by enabling electric-field-controlled spin manipulation, which circumvents conventional Joule heating effects, establishing an energy-efficient paradigm that substantially reduces dissipative losses. Recent advances in two-dimensional (2D) van der Waals (vdW) multiferroics exponentially amplify these merits through atomically thin interfaces, layer-tunable quantum confinements and gate-mediated interlayer exchange.[5,6] Such systems realize unprecedented ferroelectricity-driven interlayer magnetic coupling, where the interlayer magnetic order can be precisely manipulated *via* electric fields.[7–10] Crucially, switchable ferroelectric dipoles can reversibly invert the sign of interlayer exchange interactions, driving bistable transitions between FM and AFM orderings.[11–14] Such electrically programmable spin configurations directly modulate the tunneling electroresistance in multiferroic tunnel junctions, realizing a nonvolatile memory mechanism with dual-mode information encoding *via* polarization switching.[15–20]

Despite these extensive research studies, current multiferroic systems predominantly employ heterostructures, consisting of alternating FM and multiferroic layers, to enable ferroelectric control of interlayer magnetic coupling.[21–23] In these cases, non-centrosymmetric interfacial effects drive orbital reconstruction of magnetic atoms, leading to unequal magnetic moments in adjacent layers due to distinct chemical environments. The intrinsic interfacial asymmetry imposes a fundamental limitation on the interlayer magnetic coupling: although ferroelectric gating enables modulation between FM

*School of Physics, State Key Laboratory of Crystal Materials, Shandong University, Shandanan Str. 27, Jinan 250100, China. E-mail: lixr@sdu.edu.cn, daiy60@sdu.edu.cn, yandong.ma@sdu.edu.cn*

and ferrimagnetic (FiM) states,[24–28] the realization of a fully AFM configuration remains unattainable. Critically, unlike the FM–FiM transition, the FM–AFM transition offers distinct spintronic advantages, including magnetic-field immunity and zero net magnetization, which are essential for high-density memory integration and low-power operation.[29,30] Nevertheless, ferroelectricity-driven FM–AFM switching is strongly suppressed by the unavoidable interfacial asymmetry in conventional vdW heterostructures, presenting a central materials-design challenge.

In this work, we introduce an innovative strategy for realizing electrically tunable interlayer magnetic phase transitions in vdW homobilayers. This framework enables bidirectional switching between AFM and FM states through polarization-modulated band alignment, where ferroelectric order governs interlayer exchange interactions. The critical insight lies in symmetry-dependent charge redistribution: antiparallel polarization induces momentum-matched band alignment that enhances localized superexchange for AFM stabilization, whereas parallel polarization establishes a type-III band offset, concurrently fulfilling the Stoner criterion for delocalized electrons to establish FM order. First-principles simulations on $Tl_2NO_2$ bilayers validate this mechanism. Crucially, the AFM state exhibits simultaneous layer-polarized valley and spin Hall transport, while FM ordering suppresses these characteristics—a dichotomy enabling all-electric nonvolatile control over emergent phenomena.

## Methods

All density functional theory (DFT)[31] calculations were performed using the Vienna Ab initio Simulation Package (VASP).[32] The projector augmented-wave (PAW) method was employed to describe electron–ion interactions,[33] with the exchange–correlation functional approximated by the Perdew–Burke–Ernzerhof (PBE) formulation of the generalized gradient approximation (GGA).[34] The hybrid functional (HSE06) calculations[35] were also performed to calculate the band structures. A vacuum layer exceeding 15 Å along the out-of-plane direction was implemented to eliminate spurious interactions between periodic images. The DFT-D3 method was adopted to correct the vdW interaction.[36] The plane-wave cutoff energy was set to 520 eV, with convergence criteria of $10^{-6}$ eV for electronic iterations and 0.01 eV $Å^{-1}$ for ionic relaxation. A Monkhorst–Pack *k*-point grid of 11 × 11 × 1 was adopted for sampling the two-dimensional Brillouin zone,[37] and the ferroelectric switching barrier is obtained by the nudged elastic band (NEB) method.[38] The Berry curvature is calculated using the maximally localized Wannier functions (MLWFs) as implemented in the WANNIER90 package.[39]

## Results and discussion

Our proposed mechanism is based on a vdW homobilayer system comprising two identical multiferroic monolayers with coexisting ferroelectric and FM orders. As governed by interlayer registry symmetry, two prototypical stacking states emerge with fundamentally distinct magnetoelectric responses (Fig. 1). Specifically, in state I of centrosymmetric stacking configuration (Fig. 1a), the inversion symmetry operation ($z \rightarrow -z$) enforces antiparallel alignment of layer-polarized ferroelectric dipoles ($P_{\uparrow\downarrow}$). This compensation of built-in electric fields leads to parallel band alignment with blunt conduction/valence band edges (Fig. 1c). The preserved semiconducting electronic structure with localized charge distribution facilitates interlayer AFM ordering through

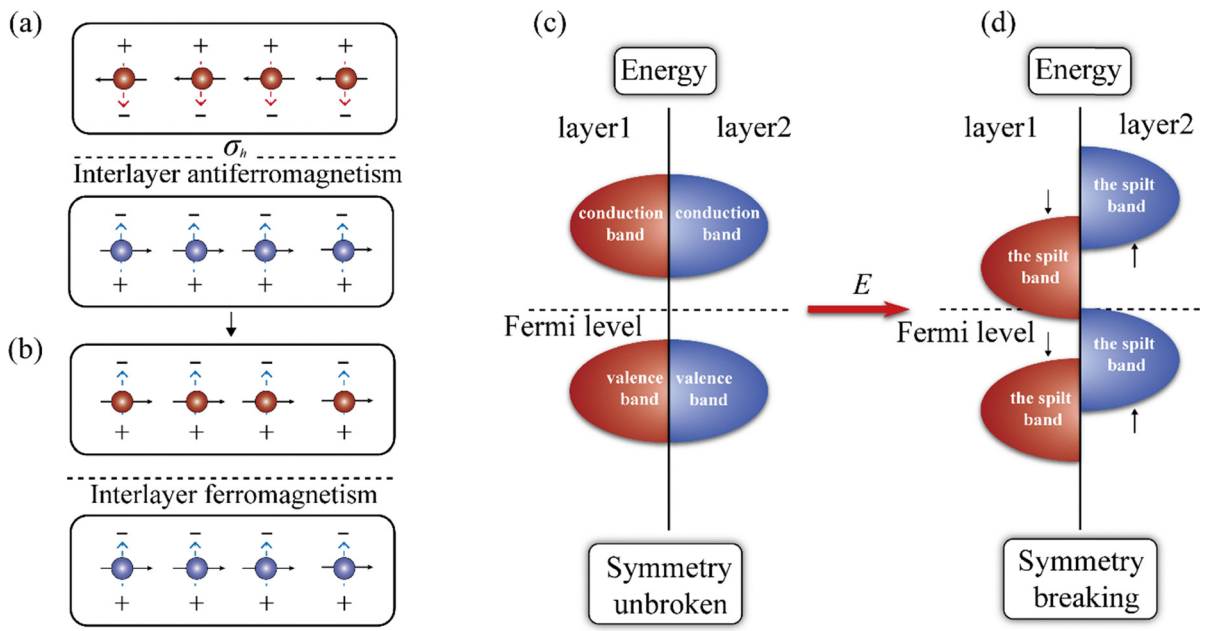


Fig. 1 Schematic diagrams of vdW multiferroic homobilayers for (a) state I with antiparallel ferroelectric polarizations ($P_{\uparrow\downarrow}$) and (b) state-II with parallel ferroelectric polarizations ($P_{\uparrow\uparrow}$), respectively. Band alignments of vdW multiferroic homobilayers for (c) state-I and (d) state-II, respectively.

competing superexchange pathways, where virtual hopping processes dominate over direct exchange interactions. In state II, the breaking of inversion symmetry in the noncentrosymmetric stacking configuration (Fig. 1b) allows cooperative alignment of ferroelectric polarizations ($P_{\uparrow\uparrow}$). The uncompensated interfacial electric field can create a type-III band alignment with staggered band edges (Fig. 1d),[40,41] generating substantial density of states (DOS) at the Fermi level ($E_F$) through hybridization of frontier orbitals. Crucially, the enhanced DOS at $E_F$ satisfies the Stoner criterion for itinerant ferromagnetism, $\eta = I{\cdot}D(E_F) > 1$. Here, $I$ represents the enhanced exchange integral due to overlapping frontier orbitals in the metallic phase, while $D(E_F)$ quantifies the boosted state density from band overlap. This criterion fulfillment triggers spontaneous spin splitting *via* kinetic exchange processes, ultimately mediating long-range interlayer FM ordering through delocalized electron screening effects.

The revealed stacking-dependent magnetic configurations enable reversible electric field switching between two states through symmetry engineering. For state I with centrosymmetry, applying an out-of-plane electric field can overcome the intrinsic polarization potential barrier, driving spontaneous polarization reorientation from antiparallel ($P_{\uparrow\downarrow}$) to parallel ($P_{\uparrow\uparrow}$) alignment, termed state II. This electric-field-induced symmetry-breaking transition transforms the interfacial dipole configuration from compensated to additive, accompanied by a semiconductor-to-metal transition as the band alignment evolves from parallel (Fig. 1c) to type-III (Fig. 1d). Crucially, the emergent metallic phase activates the Stoner criterion, dictating a magnetic phase transition from AFM to FM ordering. The reversal transition from state-II to state-I is also achievable by reversing the external electric field to destabilize parallel polarization alignment, thereby restoring ferroelectric centrosymmetry through interlayer charge redistribution, resulting in a magnetic phase transition from FM to AFM ordering. This demonstrates the realization of electric field control of interlayer magnetic phase transitions in vdW homobilayers.

A promising candidate to realize this mechanism is the $Tl_2NO_2$ monolayer.[42–44] The $Tl_2NO_2$ monolayer crystallizes in a triangular lattice with $P3m1$ space group symmetry, with a lattice parameter of 3.63 Å. Its structural configuration exhibits a stacking sequence of O–Tl–N–Tl–O, where the central N atom forms a tetrahedral coordination with three adjacent Tl atoms. The asymmetric displacement of the N atomic layer leads to different coordination environments for Tl layers, forming three long N–Tl bonds and one short N–Tl bond. The resultant polar distortion under $C_{3v}$ symmetry generates an out-of-plane

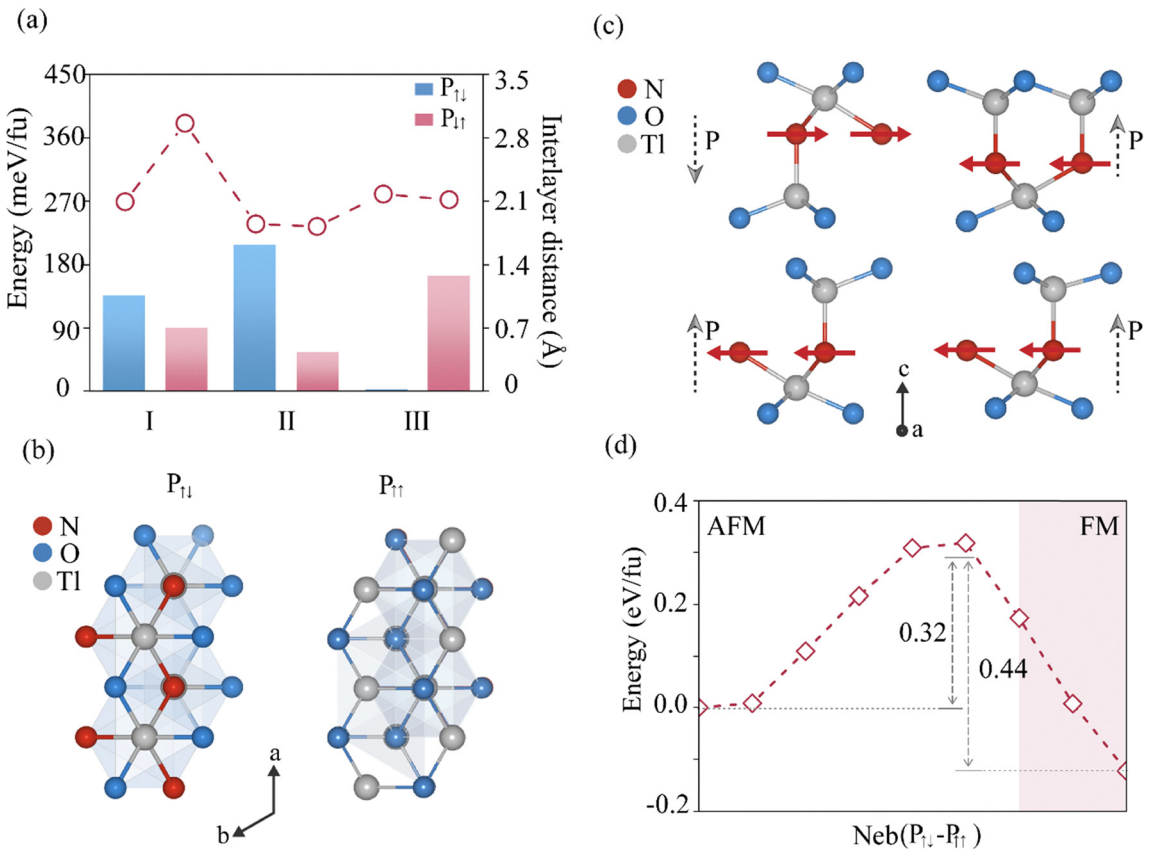


Fig. 2 (a) Total energy differences per unit cell of six representative $Tl_2NO_2$ homobilayer configurations relative to the most stable $P_{\uparrow\downarrow}$-III state, whose total energy is taken as the reference (0 eV), and the layer spacing of those configurations. (b) Top and (c) side views of the $P_{\uparrow\downarrow}$-III state and the corresponding electric-field driven $P_{\uparrow\uparrow}$ state, with red arrows indicating the spin orientations. Atomic species: Tl (silver), N (red), O (blue). (d) Ferroelectric phase transition from $P_{\uparrow\downarrow}$ to $P_{\uparrow\uparrow}$ states of the $Tl_2NO_2$ homobilayer.

spontaneous ferroelectric polarization, confirming the ferroelectric nature of the $Tl_2NO_2$ monolayer with two energetically degenerate ferroelectric states (referred to as $P_\uparrow$ and $P_\downarrow$), as shown in Fig. S1 (SI). Simultaneously, the $Tl_2NO_2$ monolayer exhibits spin-polarized character originating from N-p orbital electrons, stabilizing a ferromagnetic ground state characterized by in-plane magnetic anisotropy. The coexistence of ferroelectric and FM nature suggests the $Tl_2NO_2$ monolayer as a 2D multiferroic system.

Following the proposed mechanism, we first construct a $Tl_2NO_2$ homobilayer with the constituent layers carrying opposite ferroelectric polarizations, *i.e.*, $P_{\uparrow\downarrow}$ and $P_{\downarrow\uparrow}$. To estimate the most stable configuration, we consider three high-symmetric stacking arrangements for both $P_{\uparrow\downarrow}$ and $P_{\downarrow\uparrow}$: (i) in stacking-I, the N atoms of the top and bottom layers are vertically aligned; (ii) in stacking-II, the top-layer N atom aligns vertically with an outer O atom of the bottom layer; and (iii) in stacking-III, the top-layer N atom aligns vertically with an inner O atom of the bottom layer. The crystal structures of these six configurations are displayed in Fig. S2. From Fig. 2a, we can see that the most stable configuration of the $Tl_2NO_2$ homobilayer corresponds to $P_{\uparrow\downarrow}$ arrangement in stacking-III. Therefore, we focus our subsequent analysis on this ground-state configuration. Upon applying an external electric field, $P_{\uparrow\downarrow}$ can be transformed into $P_{\uparrow\uparrow}$. The corresponding structure of $P_{\uparrow\uparrow}$ is displayed in Fig. 2b. We determine their corresponding magnetic ground states by evaluating both AFM and FM interlayer couplings. As shown in Fig. 2c, $P_{\uparrow\downarrow}$ exhibits AFM interlayer coupling with an energy lowering of 2.14 meV per unit cell over the FM interlayer case. Remarkably, when the FE polarization switches from $P_{\uparrow\downarrow}$ to $P_{\uparrow\uparrow}$, the interlayer magnetic coupling undergoes a transition from AFM to FM ordering, energetically favored by 9.62 meV per unit cell. This demonstrates the direct control of the interlayer magnetic ground state through ferroelectric polarization switching in the $Tl_2NO_2$ homobilayer. The test calculations show that in the same stacking arrangement, the interlayer magnetic coupling has negligible influence on the interlayer distance.

To assess the feasibility of the FE switching between $P_{\uparrow\downarrow}$ and $P_{\uparrow\uparrow}$ states, we calculate the transition pathway and associated switching energy barrier. Significantly, the lowest-energy switching path preserves the interlayer registry, avoiding vdW bond disruption and thus yielding a minimal activation barrier. As depicted in Fig. 2d, the NEB calculations identify a surmountable switching barrier of 0.34 eV $fu^{-1}$, smaller than 0.52 eV $fu^{-1}$ reported for a $Sc_2CO_2$ monolayer,[45] confirming

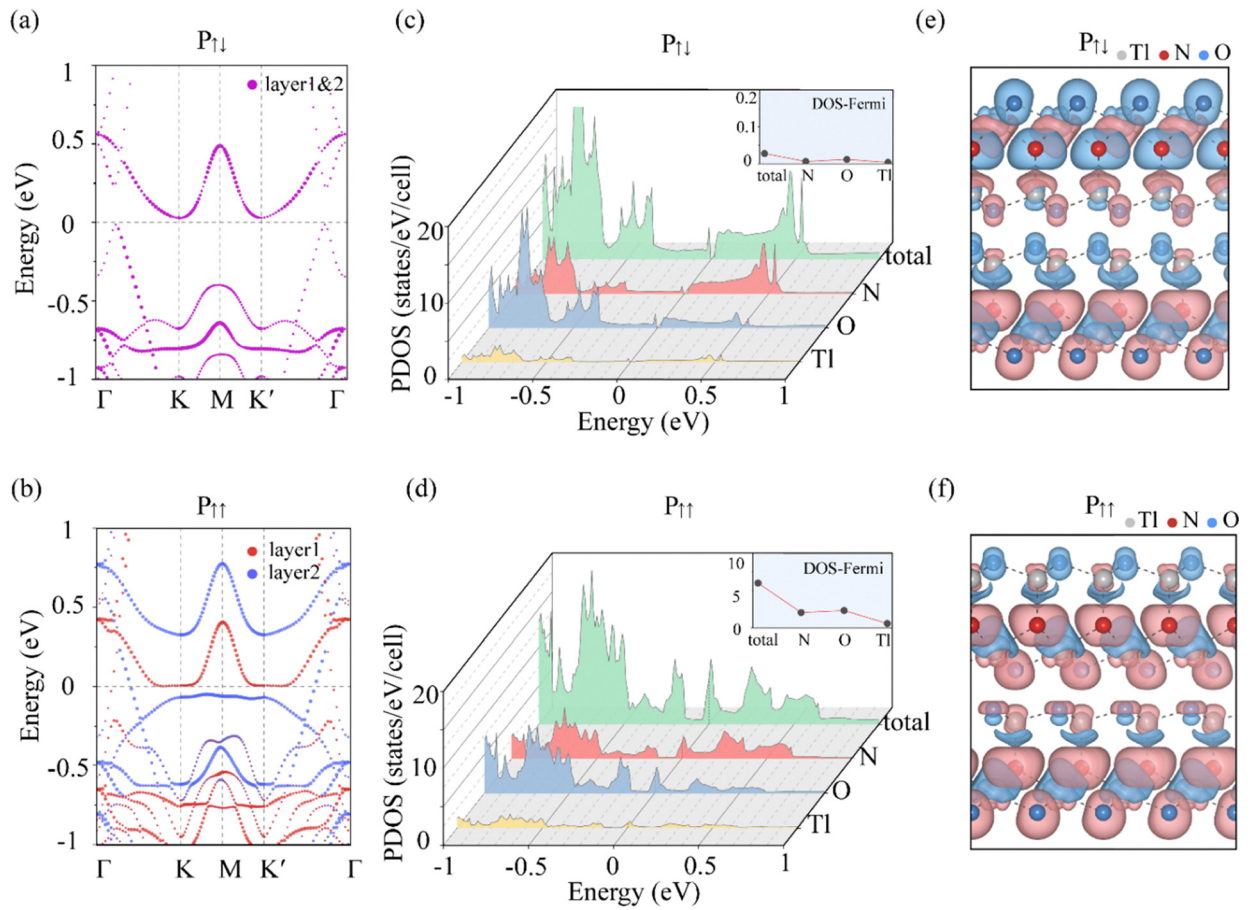


Fig. 3 (a) and (b) Layer-projected band structures for $P_{\uparrow\downarrow}$ and $P_{\uparrow\uparrow}$ states under magnetic ground states. (c) and (d) Non-spin-polarized atom-projected DOS for $P_{\uparrow\downarrow}$ and $P_{\uparrow\uparrow}$ states, with insets showing DOS at the Fermi level. (e) and (f) Spin charge densities for $P_{\uparrow\downarrow}$ and $P_{\uparrow\uparrow}$ states, where red and blue colors represent spin-up and spin-down components, respectively.

the possibility of electric-field-driven switching. Notably, the switched $P_{\uparrow\uparrow}$ state with FM coupling is energetically favorable, exhibiting a 0.24 eV stabilization compared to the initial $P_{\uparrow\downarrow}$ state with AFM coupling. These results conclusively demonstrate electric-field control of interlayer magnetic coupling in the $Tl_2NO_2$ homobilayer.

To validate the ferroelectricity-driven interlayer magnetic coupling transition in the $Tl_2NO_2$ homobilayer, we systematically analyze the electronic and magnetic properties of $P_{\uparrow\downarrow}$ and $P_{\uparrow\uparrow}$. Fig. 3a reveals that $P_{\uparrow\downarrow}$ forms an indirect semiconductor with a narrow band gap of 42 meV, where the valence band maximum (VBM) lies between Γ and K/K′ points, while the conduction band minimum (CBM) comprises two degenerate valleys at K and K′. The layer-projected bands show blunt alignment between top and bottom layers. In striking contrast, as illustrated in Fig. 3b, $P_{\uparrow\uparrow}$ displays metallic behavior with staggered band alignments between top and bottom layers. These are in good agreement with the proposed mechanism. HSE06 calculations demonstrate that the type-III band alignment persists for the $Tl_2NO_2$ homobilayer with $P_{\uparrow\uparrow}$ (Fig. S4). Remarkably, spin–orbit coupling (SOC) lifts the degeneracy of the interlayer-hybridized states and induces band reconstruction near the Fermi level, creating flat bands tightly pinned to the Fermi level. In the homobilayer system, the synergistic effect of parallel FE polarization and interlayer coupling drives the formation of a type-III band alignment. This alignment results in the energetic overlap between the conduction band of one layer and the valence band of the other layer, creating a high DOS near the Fermi level. Crucially, the inclusion of SOC lifts the degeneracy of these states originating from the type-III overlap. The strong interlayer hybridization combined with SOC leads to the formation of flat bands with exceptionally weak dispersion. Due to the metallic nature of the homobilayer with $P_{\uparrow\uparrow}$, these flat bands reside at the Fermi level. Band structure calculations for FM states with $P_{\uparrow\uparrow}$ in both stacking-I and stacking-II configurations are also presented in Fig. S5. Both stacking arrangements with $P_{\uparrow\uparrow}$ adopt FM ground states with metallic type-III band alignment. However, the degree of band offset varies across stackings due to distinct interlayer chemical environments, which modulates the strength of interlayer coupling. This can directly impact the DOS near the Fermi level. To isolate the effects of ferroelectric polarization arrangements on the electronic structures, we calculate the non-spin-polarized DOS for both $P_{\uparrow\downarrow}$ and $P_{\uparrow\uparrow}$ states. Fig. 3c reveals that $P_{\uparrow\downarrow}$ maintains its semiconducting character with vanishing DOS at the Fermi level, consistent with its aligned band structure. In contrast, $P_{\uparrow\uparrow}$ exhibits metallic behavior due to the interlayer staggered band offset, showing a sharp DOS peak at the Fermi level, as shown in Fig. 3d. Data analysis reveals that the ferroelectric switching from $P_{\uparrow\downarrow}$ to $P_{\uparrow\uparrow}$ induces a dramatic enhancement of the Fermi-level DOS from 0 to 6.01 states per eV, directly linking the polarization orientation to the emergent metallicity.

We further establish the microscopic connection between ferroelectric ordering and interlayer magnetic coupling. In the metallic $P_{\uparrow\uparrow}$ where itinerant electrons dominate the interlayer magnetic coupling, we employ the Stoner criterion $\eta = I \cdot D(E_F)$,[46] where $I = \Delta E_{ex}/m$. Here, $\Delta E_{ex}$ denotes the average spin splitting from band structure calculations, with a value of 1.1 eV, and $m$ represents the average magnetic moment per unit cell, with a value of 2.08 $\mu_B$. For the metallic $P_{\uparrow\uparrow}$, we obtain $\eta = 3.18 > 1$, satisfying the Stoner condition for interlayer FM coupling. In contrast, the semiconducting $P_{\uparrow\downarrow}$ with $D(E_F) = 0$ naturally favors interlayer AFM coupling with localized orbital contributions instead of itinerant electrons. This interpretation is further supported by the spin charge density analysis shown in Fig. 3e and f, which reveals distinct magnetization distributions for the two magnetic ground states. In the semiconducting $P_{\uparrow\downarrow}$, the half-filled p orbitals of N atoms mediate AFM superexchange through saturated p bridges from O and Tl atoms, forming robust interlayer AFM coupling that is insensitive to bond angles and intermediate atom numbers. This dual mechanism, comprising itinerant-electron-driven ferromagnetism and localized-orbital-mediated antiferromagnetism, establishes a complete picture of electric-field control of interlayer magnetic coupling.

Beyond the electric-field control of interlayer magnetic coupling mechanisms, we further investigate valley-dependent phenomena in the AFM ordered $P_{\uparrow\downarrow}$ state. While the ground state exhibits in-plane interlayer antiferromagnetism that preserves K/K′ valley degeneracy (Fig. 3a), the exceptionally small magnetic anisotropy energy ($MAE_{z-x}$ = 0.27 meV) enables facile reorientation of magnetization to the out-of-plane direction under external stimuli. This pronounced tunability prompts our examination of valley polarization effects under out-of-plane magnetization, where the SOC is expected to lift the valley degeneracy in the AFM ordered $P_{\uparrow\downarrow}$. In the AFM ordered $P_{\uparrow\downarrow}$, the hexagonal lattice comprises two triangular sublattices (A and B) with opposing net magnetic moments, breaking individual inversion ($\mathcal{P}$) and time-reversal ($\mathcal{T}$) symmetries while preserving combined $\mathcal{PT}$ symmetry. When operating on a Bloch state, $\mathcal{PT}$ symmetry preserves its wavevector while inverting the spin. Consequently, the Bloch states of the same K and opposite spins are degenerate.[47–49] The valley features can be described by solving the Schrödinger equation incorporating SOC terms. Taking the out-of-plane direction as the $z$-axis, we first express the SOC Hamiltonian in spherical coordinates:

$$H = \frac{\lambda}{2}(\hat{S}^+ + \hat{S}^-)\left(-\hat{L}_z \sin\theta + \frac{1}{2}\hat{L}_+ e^{-i\phi\cos\theta} + \frac{1}{2}\hat{L}_- e^{i\phi\cos\theta}\right)$$

Here, $\hat{S}^+$ and $\hat{S}^-$ denote spin raising/lowering operators, $\hat{L}_\pm$ are orbital angular momentum ladder operators, and $\hat{L}_z$ represents the $z$-component of orbital angular momentum. The coupling constant $\lambda$ quantifies the SOC strength, while $\theta$ and $\phi$ are spherical coordinate angles that define the spin orientation.

At the K and K′ valleys, the wavefunctions primarily originate from hybridization of the $p_x$ and $p_y$ orbitals of N atoms and the $p_z$ orbitals of O atoms as analyzed from the orbital-resolved bands in Fig. S3. Considering $\mathcal{T}$ symmetry constraints on interorbital phase differences at these high-symmetry points,

the normalized wavefunctions can be expressed as:

$$|\psi_c^\tau\rangle = \frac{1}{\sqrt{6}}[|p_x, s, m_s\rangle + |p_y, s, m_s\rangle + 2i\tau|p_z, s, m_s\rangle]$$

where $\tau = \pm 1$ denotes the valley index, $|p_x\rangle$ and $|p_y\rangle$ represent N-atom p orbitals, $|p_z\rangle$ corresponds to the O-atom p orbital, and $|s, m_s\rangle$ describe spin states. Omitting spin terms for simplicity:

$$|\psi_c^\tau\rangle = \frac{1}{\sqrt{6}}[|p_x\rangle + |p_y\rangle + 2i\tau|p_z\rangle]$$

The SOC-induced energy splitting between valleys is obtained through expectation value calculations:

$$E_c^+ = \langle\psi_c^+|H|\psi_c^+\rangle$$

$$E_c^- = \langle\psi_c^-|H|\psi_c^-\rangle$$

The valley splitting energy is evaluated as:

$$\begin{aligned}\Delta E &= \langle E_c^+ - E_c^- \rangle \\ &= 8i[\langle p_x|H|p_z\rangle + \langle p_y|H|p_z\rangle - \langle p_z|H|p_x\rangle]\frac{1}{6} \\ &= \frac{4}{3}\lambda\hbar^2\cos\theta\end{aligned}$$

This demonstrates that valley polarization reaches its maximum when magnetization aligns with the out-of-plane direction ($\theta = 0$). Our calculations indeed show that it has a spontaneous valley polarization of $\Delta E = 16.2$ meV, as shown in Fig. 4b.

To elucidate valley-contrasted physics in the out-of-plane magnetized bilayer, we calculate spin-resolved Berry curvature distributions using the Kubo formula:

$$\Omega(k) = -\sum_n \sum_{n' \neq n} f_n \frac{2\mathrm{Im}\langle\psi_{nk}|\hat{v}_x|\psi_{n'k}\rangle\langle\psi_{n'k}|\hat{v}_y|\psi_{nk}\rangle}{(E_n - E_{n'})^2}$$

where $f_n$ is the Fermi–Dirac distribution, $\psi_{nk}$ denotes the Bloch eigenstate with energy $E_n$, and $\hat{v}_{x/y}$ represents the velocity operator along the $x/y$ direction. The calculated Berry curvatures of the spin-up and spin-down channels of the $Tl_2NO_2$ homobilayer in the 2D Brillion zone as counter maps are illustrated in Fig. 4c. The K and K′ valleys exhibit opposite Berry curvatures for a given spin channel. Due to the $\mathcal{PT}$ symmetry of the $Tl_2NO_2$ homobilayer with $P_{\uparrow\downarrow}$ under the AFM state, the valley index is not an independent degree of freedom, but is defined by the operator $s\cdot\tau$, where $s$ is spin and $\tau$ is valley pseudospin.[49] While the spin degeneracy dictates a vanishing total Berry curvature, spin-resolved contributions associated with a specific valley state for a given spin polarization exhibit a non-vanishing hidden Berry curvature.[50] Consequently, these spin–valley locked hidden Berry curvatures allow for the possibility of independently addressing valley states with distinct spin orientations *via* selective optical pumping or external electric fields. These selective manipulations could generate a measurable spin-resolved anomalous Hall conductivity (AHC).[51] Owing to the nonzero Berry curvature, an in-plane electric field induces transverse carrier velocities $v \approx E \times \Omega(k)$, exhibiting valley-dependent directional selectivity. When shifting the Fermi level between the K and K′ valleys in the conduction band and applying an in-plane electric field, carriers with $(\tau, s) = (-1, \pm 1/2)$ accumulate and undergo spin-dependent transverse separation.[52,53] Given the layer-projected spin polarization near high-symmetry points, this generates a layer-polarized valley and spin Hall effect (Fig. 4d),[54] where counter-propagating edge channels emerge with distinct layer and spin indices. To enable the experimental detection of the AHC arising from the manipulation of these hidden Berry curvatures, we introduce a feasible approach to explicitly break the $\mathcal{PT}$ symmetry by applying a vertical electric field (magnitude: 0.005 V Å$^{-1}$). The calculated AHC is shown in Fig. S6.

## Conclusions

In summary, we propose an unconventional mechanism for electrically controlled interlayer magnetic phase switching in homobilayer systems, realized through ferroelectric polarization-dependent band engineering. The switching arises from

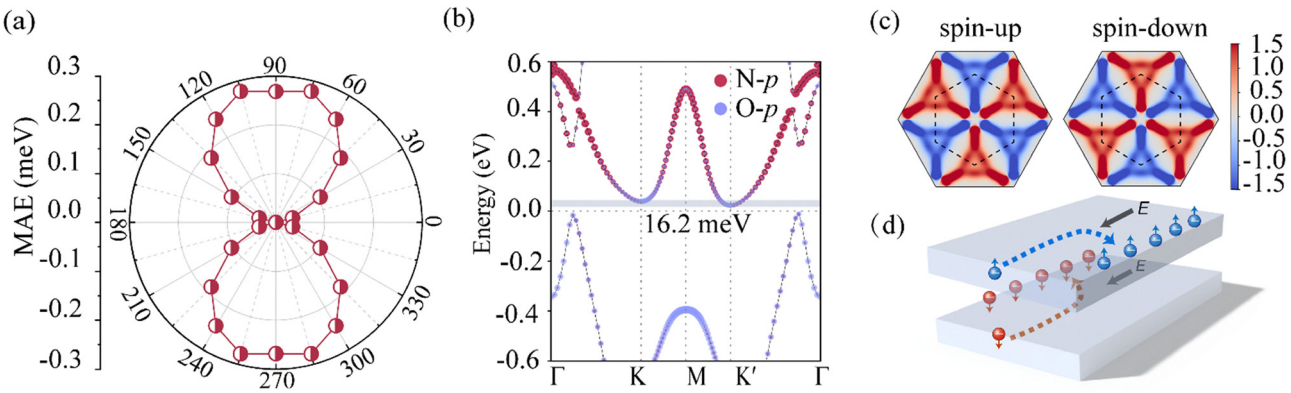


Fig. 4 (a) Magnetic anisotropy energy (MAE) of $P_{\uparrow\downarrow}$ under the AFM state for the $Tl_2NO_2$ homobilayer. (b) Valley-polarized band structure with out-of-plane magnetization. (c) Berry curvature of partial spins in the 2D Brillouin zone. (d) Schematic diagram of layer-polarized valley and spin Hall effects.

symmetry-breaking interlayer charge transfer: antiparallel ferroelectric polarization enforces parallel band alignment that favors AFM interlayer coupling *via* local superexchange, while parallel polarization induces a type-III band alignment that satisfies the Stoner criterion, thereby stabilizing FM ordering. First-principles calculations on the $Tl_2NO_2$ homobilayer confirm the viability of this approach. Importantly, the AFM phase supports coexisting layer-polarized valley and spin Hall currents, whereas these features become mutually exclusive in the FM state. Our results demonstrate a nonvolatile route for controlling both valley and spin degrees of freedom *via* ferroelectric switching, offering a promising platform for multifunctional spintronic and valleytronic applications.

## Conflicts of interest

The authors declare no competing financial interests.

## Data availability

The data supporting this article have been included as part of the SI.

Details regarding the geometric structures of the $Tl_2NO_2$ monolayer, six configurations under different ferroelectric arrangements of $Tl_2NO_2$ homobilayers, element-resolved and orbital-resolved band structures of $Tl_2NO_2$ homobilayers with $P_{\uparrow\downarrow}$-III under out-of-plane magnetization, band structures of $Tl_2NO_2$ homobilayers with $P_{\uparrow\downarrow}$-III and $P_{\uparrow\uparrow}$-III calculated using HSE06, band structures of $Tl_2NO_2$ homobilayers with $P_{\uparrow\uparrow}$-I and $P_{\uparrow\uparrow}$-II, band structure of the $Tl_2NO_2$ homobilayer with $P_{\uparrow\downarrow}$-III after breaking PT symmetry with a vertical electric field and its corresponding AHC, and the symmetry information, Wyckoff positions, atomic coordinates of the $Tl_2NO_2$ homobilayers and monolayer. See DOI: **https://doi.org/10.1039/d5mh01095k**

## Acknowledgements

This work was supported by the National Natural Science Foundation of China (12274261), the Taishan Young Scholar Program of Shandong Province, and the Shandong Provincial Natural Science Foundation of China (ZR2024QA016).

## References

1 N. Hur, S. Park, P. A. Sharma, J. S. Ahn, S. Guha and S.-W. Cheong, Electric polarization reversal and memory in a multiferroic material induced by magnetic fields, *Nature*, 2004, **429**, 392.
2 C. Gong, E. M. Kim, Y. Wang, G. Lee and X. Zhang, Multiferroicity in atomic van der Waals heterostructures, *Nat. Commun.*, 2019, **10**, 2657.
3 S. Dong, J. M. Liu, S.-W. Cheong and Z. Ren, Multiferroic materials and magnetoelectric physics: Symmetry, entanglement, excitation, and topology, *Adv. Phys.*, 2015, **64**, 519.
4 Y. Zhao, J. J. Zhang, S. Yuan and Z. Chen, Nonvolatile electrical control and heterointerface-induced half-metallicity of 2D ferromagnets, *Adv. Funct. Mater.*, 2019, **29**, 1901420.
5 Y. Su, X. Li, M. Zhu, J. Zhang, L. You and E. Y. Tsymbal, van der Waals multiferroic tunnel junctions, *Nano Lett.*, 2021, **21**, 175.
6 C. Wang, L. You, D. Cobden and J. Wang, Towards two-dimensional van der Waals ferroelectrics, *Nat. Mater.*, 2023, **22**, 542.
7 Y. Zhang, M. G. Han, J. A. Garlow, Y. Tan, F. Xue, L.-Q. Chen, P. Munroe, N. Valanoor and Y. Zhu, Deterministic ferroelastic domain switching using ferroelectric bilayers, *Nano Lett.*, 2019, **19**, 5319.
8 X. L. Wang, *et al.*, Electrical and magnetic anisotropies in van der Waals multiferroic $CuCrP_2S_6$, *Nat. Commun.*, 2023, **14**, 840.
9 W. Li, *et al.*, Emergence of ferroelectricity in a nonferroelectric monolayer, *Nat. Commun.*, 2023, **14**, 2757.
10 X. Zhang, B. Yang, X. Guo, Y. Liu, X. Han and Y. Yan, Ferroelectric control of magnetic coupling of monolayer $MnBr_2$ in semiconducting multiferroic van der Waals heterostructure, *Appl. Surf. Sci.*, 2023, **614**, 156201.
11 X. Zhang, Z. Zhou, X. Yu, Y. Guo, Y. Chen and J. Wang, Ferroelectric control of polarity of the spin-polarized current in van der Waals multiferroic heterostructures, *Adv. Funct. Mater.*, 2023, **33**, 2301353.
12 H. Ju, *et al.*, Possible persistence of multiferroic order down to bilayer limit of van der Waals material $NiI_2$, *Nano Lett.*, 2021, **21**, 5126.
13 X. X. Shi, X. Q. Liu and X. M. Chen, Readdressing of magnetoelectric effect in bulk $BiFeO_3$, *Adv. Funct. Mater.*, 2017, **27**, 1604037.
14 K. Liu, X. Ma, S. Xu, Y. Li and M. Zhao, Tunable sliding ferroelectricity and magnetoelectric coupling in two-dimensional multiferroic MnSe materials, *npj Comput. Mater.*, 2023, **9**, 16.
15 J. Pan, Y. F. Zhang, Y. Y. Zhang and S. Du, Engineering two-dimensional magnetic heterostructures: A theoretical perspective, *Nano Lett.*, 2024, **24**, 14909.
16 M. Xu, C. Huang, Y. Li, S. Liu, X. Zhong, P. Jena, E. Kan and Y. Wang, Electrical control of magnetic phase transition in a type-I multiferroic double-metal trihalide monolayer, *Phys. Rev. Lett.*, 2020, **124**, 067602.
17 N. Sivadas, S. Okamoto, X. Xu, C. J. Fennie and D. Xiao, Stacking-dependent magnetism in bilayer $CrI_3$, *Nano Lett.*, 2018, **18**, 7658.
18 Y. Niu, Z. Liu, K. Wang, W. Ai, T. Gong, T. Liu, L. Bi, G. Zhang, L. Deng and B. Peng, Robust electric-field control of colossal exchange bias in $CrI_3$ homotrilayer, *Adv. Mater.*, 2024, **36**, 2403066.
19 H. B. Chen, Y. Zhou and Y. Q. Li, Bond distortion effects and electric orders in spiral multiferroic magnets, *J. Phys.: Condens. Matter*, 2013, **25**, 286004.
20 P. Kavle, A. M. Ross, J. A. Zorn, P. Behera, E. Parsonnet, X. Huang, C.-C. Lin, L. Caretta, L.-Q. Chen and L. W. Martin, Exchange-interaction-like behavior in ferroelectric bilayers, *Adv. Mater.*, 2023, **35**, 2301934.

21 T. Taniyama, Y. Gohda, K. Hamaya and T. Kimura, Artificial multiferroic heterostructures—Electric field effects and their perspectives, *Sci. Technol. Adv. Mater.*, 2024, **25**, 2412970.
22 S. K. Chakraborty, B. Kundu, B. Nayak, S. P. Dash and P. K. Sahoo, Challenges and opportunities in 2D heterostructures for electronic and optoelectronic devices, *iScience*, 2022, **25**, 103942.
23 J. M. Hu, L. Q. Chen and C.-W. Nan, Multiferroic heterostructures integrating ferroelectric and magnetic materials, *Adv. Mater.*, 2016, **28**, 15.
24 Y. Li, T. Hu, P. Guo and W. Ren, Nonvolatile multiferroic coupling in van der Waals heterostructure, *Appl. Phys. Lett.*, 2023, **123**, 142904.
25 S. Jiang, J. Shan and K. F. Mak, Electric-field switching of two-dimensional van der Waals magnets, *Nat. Mater.*, 2018, **17**, 406.
26 X. Xu and L. Yang, Enhanced magnetoelectric coupling in two-dimensional hybrid multiferroic heterostructures, *Phys. Rev. B*, 2024, **110**, 165408.
27 Y. Wang, X. Xu, X. Zhao, W. Ji, Q. Cao, S. Li and Y. Li, Switchable half-metallicity in A-type antiferromagnetic $NiI_2$ bilayer coupled with ferroelectric $In_2Se_3$, *npj Comput. Mater.*, 2022, **8**, 1.
28 W. Luo, K. Xu and H. Xiang, Two-dimensional hyperferroelectric metals: A different route to ferromagnetic–ferroelectric multiferroics, *Phys. Rev. B*, 2017, **96**, 235415.
29 T. Jungwirth, X. Marti, P. Wadley and J. Wunderlich, Antiferromagnetic spintronics, *Nat. Nanotechnol.*, 2016, **11**, 231.
30 D. L. Duong, S. J. Yun and Y. H. Lee, van der Waals layered materials: Opportunities and challenges, *ACS Nano*, 2017, **11**, 11803.
31 W. Kohn and L. J. Sham, Self-consistent equations including exchange and correlation effects, *Phys. Rev.*, 1965, **140**, A1133.
32 G. Kresse and J. Furthmüller, Efficient iterative schemes for *ab initio* total-energy calculations using a plane-wave basis set, *Phys. Rev. B: Condens. Matter Mater. Phys.*, 1996, **54**, 11169.
33 P. E. Blöchl, Projector augmented-wave method, *Phys. Rev. B: Condens. Matter Mater. Phys.*, 1994, **50**, 17953.
34 J. P. Perdew, K. Burke and M. Ernzerhof, Generalized gradient approximation made simple, *Phys. Rev. Lett.*, 1996, **77**, 3865.
35 J. Heyd, G. E. Scuseria and M. Ernzerhof, Hybrid functionals based on a screened coulomb potential, *J. Chem. Phys.*, 2003, **118**, 8207.
36 S. Grimme, J. Antony, S. Ehrlich and H. Krieg, A consistent and accurate ab initio parametrization of density functional dispersion correction (DFT-D) for the 94 elements H-pu, *J. Chem. Phys.*, 2010, **132**, 154104.
37 H. J. Monkhorst and J. D. Pack, Special points for Brillouin-zone integrations, *Phys. Rev. B*, 1976, **13**, 5188.
38 J. Neugebauer and M. Scheffler, Adsorbate-substrate and adsorbate-adsorbate interactions of Na and K adlayers on Al(111), *Phys. Rev. B: Condens. Matter Mater. Phys.*, 1992, **46**, 16067.
39 G. Pizzi, V. Vitale, R. Arita, S. Blügel, F. Freimuth, G. Géranton, M. Gibertini, D. Gresch, C. Johnson and T. Koretsune, Wannier90 as a community code: New features and applications, *J. Phys.: Condens. Matter*, 2020, **32**, 165902.
40 N. R. Chebrolu, B. L. Chittari and J. Jung, Flat bands in twisted double bilayer graphene, *Phys. Rev. B*, 2019, **99**, 235417.
41 T. Chu, H. Ilatikhameneh, G. Klimeck, R. Rahman and Z. Chen, Electrically tunable bandgaps in bilayer $MoS_2$, *Nano Lett.*, 2015, **15**, 8000.
42 W. Du, Z. He, K. Dou, X. Li, Y. Dai, B. Huang and Y. Ma, Chiral magnetic quasiparticles with zero topological charge in 2D lattice, *Adv. Funct. Mater.*, 2024, **34**, 2400971.
43 H. Ai, F. Li, H. Bai, D. Liu, K. H. Lo, S. A. Yang, Y. Kawazoe and H. Pan, Ferroelectricity coexisted with p-orbital ferromagnetism and metallicity in two-dimensional metal oxynitrides, *npj Comput. Mater.*, 2022, **8**, 60.
44 S. Zhang, X. Zhang, Z. He, L. Jin, C. Liu, Y. Liu and G. Liu, Weyl nodal lines, Weyl points and the tunable quantum anomalous Hall effect in two-dimensional multiferroic metal oxynitride: $Tl_2NO_2$, *Nanoscale*, 2023, **15**, 14018.
45 Y. Feng, J. Zhao, Y. Dai, B. Huang and Y. Ma, A typical breathing driven two-dimensional valley multiferroicity, *Mater. Horiz.*, 2024, **11**, 6391.
46 F. Wang, M. Xu, X. Zhou, C. Huang, J. Hao and Y. Li, Stoner ferromagnetism in intrinsic $BeC_5$ monolayer, *ACS Mater. Lett.*, 2024, **6**, 36.
47 L. Du, T. Hasan, A. Castellanos-Gomez, G.-B. Liu, Y. Yao, C. N. Lau and Z. Sun, Engineering symmetry breaking in 2D layered materials, *Nat. Rev. Phys.*, 2021, **3**, 193.
48 Y. Liu, Y. Feng, T. Zhang, Z. He, Y. Dai, B. Huang and Y. Ma, Strain-valley coupling in 2D antiferromagnetic lattice, *Adv. Funct. Mater.*, 2023, **33**, 2305130.
49 X. Li, T. Cao and Q. Niu, *et al.*, Coupling the valley degree of freedom to antiferromagnetic order, *Proc. Natl. Acad. Sci. U. S. A.*, 2013, **110**, 3738.
50 R. Chen, H. P. Sun and M. Gu, *et al.*, Layer Hall effect induced by hidden Berry curvature in antiferromagnetic insulators, *Natl. Sci. Rev.*, 2022, **11**, nwac140.
51 S. Cho, J.-H. Park, J. Hong, J. Jung, B. S. Kim, G. Han, W. Kyung, Y. Kim and S.-K. Mo, *et al.*, Experimental Observation of Hidden Berry Curvature in Inversion-Symmetric Bulk 2H-$WSe_2$, *Phys. Rev. Lett.*, 2018, **121**, 186401.
52 Y. Xu, H. Liu, Y. Dai, B. Huang and W. Wei, Spin-valley splitting and spontaneous valley polarization in antiferromagnetic $Mn_2P_2X_3Y_3$ monolayers, *Appl. Phys. Lett.*, 2023, **122**, 242404.
53 J. R. Schaibley, H. Yu, G. Clark, P. Rivera, J. S. Ross, K. L. Seyler, W. Yao and X. Xu, Valleytronics in 2D materials, *Nat. Rev. Mater.*, 2016, **1**, 1.
54 S. D. Guo, W. Xu, Y. Xue, G. Zhu and Y. S. Ang, Layer-locked anomalous valley Hall effect in a two-dimensional A-type tetragonal antiferromagnetic insulator, *Phys. Rev. B*, 2024, **109**, 134426.

 